Delft University of Technology

Effects of Exhaust Plume and Nozzle Length on Compressible Base Flows

van Gent, Paul; Payanda, Qais; Brust, Steve; van Oudheusden, Bas; Schrijer, Ferdinand

DOI
10.2514/1.J057314

Publication date
2019

Document Version
Final published version

Published in
AIAA Journal: devoted to aerospace research and development

Citation (APA)
van Gent, P., Payanda, Q., Brust, S., van Oudheusden, B., & Schrijer, F. (2019). Effects of Exhaust Plume and Nozzle Length on Compressible Base Flows. *AIAA Journal: devoted to aerospace research and development*, *57*(3), 1184-1199. https://doi.org/10.2514/1.J057314

AIAA JOURNAL
Vol. 57, No. 3, March 2019

Effects of Exhaust Plume and Nozzle Length on Compressible Base Flows

Paul L. van Gent,[*] Qais Payanda,[†] Steve G. Brust,[†] Bas W. van Oudheusden,[‡] and
Ferry F. J. Schrijer[§]
Delft University of Technology, 2629 HS Delft, The Netherlands

DOI: 10.2514/1.J057314

The effects of an exhaust plume and nozzle length on the flow organization of axisymmetric base flows have been studied experimentally at Mach numbers of 0.76 and 2.2 using particle image velocimetry. From the measured velocity data, the mean pressure field was computed. The application of different nozzle lengths resulted in flow cases in which the shear layer impinges on the model, on the flow downstream of the model, or intermittently on the model and on the flow. The results showed that, for intermediate nozzle lengths, the overall pressure level downstream of the base decreased in the transonic flow cases and increased in the supersonic flow cases, indicating an entrainment effect in transonic flow and a displacement effect in supersonic flow. An increase in nozzle length was found to lead to a higher local pressure at the nozzle exit, which seemed to result in more overexpanded plumes in the transonic flow cases and less underexpanded plumes in the supersonic flow cases.

Nomenclature

A = cross-sectional nozzle area, m^2
C_p = pressure coefficient
D = main body diameter, m
k = turbulent kinetic energy, $\mathrm{m}^2 \cdot \mathrm{s}^{-2}$
L = length of afterbody, m
M = Mach number
N = ensemble size
p = pressure, Pa
R = specific gas constant
T = temperature, K
U = velocity, $\mathrm{m} \cdot \mathrm{s}^{-1}$
γ = ratio of specific heats
σ = standard deviation of subscripted variable

Subscripts

e = condition at nozzle exit
p = condition of plume flow after isentropic expansion to the freestream pressure
ref = point of reference at the main body of the model
0 = total condition
$*$ = sonic condition
∞ = freestream condition

I. Introduction

DURING the ascent of a launch vehicle, its nozzle and other structures near the base are subject to severe mechanical and thermal loads. The relatively low pressure in the base region contributes significantly to the overall drag of the vehicle. In addition, the large-scale unsteadiness of the flow gives rise to fluctuating pressure-induced side loads on the nozzle. In particular, during transonic flight, the low-frequency component of these side loads may excite a structural response (buffeting) that introduces the risk of potential structural failure. On top of that, the entrainment of hot exhaust gasses in the recirculation region may lead to significant heat loads. The quantification of pressure and heat loads is therefore essential for the safe and efficient design of launch vehicles.

The geometry of the launcher base can be simplified to a cylindrical main body and a cylindrical afterbody with a smaller diameter that represent the main stage and nozzle, respectively. Although a number of studies have considered realistic scale models (e.g., [1]), the use of such a generic geometry facilitates the comparison and generalization of results and is therefore a more common practice in the context of more fundamental research. To illustrate the typical base flow topology, Fig. 1 shows cross-sectional views of generic subsonic and supersonic axisymmetric base flows with afterbodies and plumes (based on [2,3]). Compression–expansion systems internal to the plumes are not shown.

Due to the abrupt change in geometry, the flow separates at the trailing edge of the main body. A recirculation region is formed that is separated from the outer flow by a shear layer. Depending on the length of the afterbody (the design of the launcher), the shear layer impinges on the afterbody (nozzle) or on the flow further downstream. A special situation exists if, in view of the unsteadiness of the flow, the reattachment intermittently occurs on the afterbody and on the flow. During the ascent of the launch vehicle, the Mach number of the external flow increases. Meanwhile the typical plume state at the nozzle exit changes from initially overexpanded to increasingly underexpanded because of a decrease in ambient pressure. Based on the launch profile of the Ariane 5 [4,5], the transition to an underexpanded plume occurs at about a 14 km height when the launcher travels at about Mach 1.9. When the flow becomes supersonic, a Prandtl–Meyer expansion fan is formed at the trailing edge of the main body, whereas a shock wave is formed at reattachment as the flow is deflected back in the direction of the freestream flow (see Fig. 1b). An additional shock wave may form at the nozzle exit, depending on the plume conditions and the nozzle length [6].

The presence of an exhaust plume causes displacement of the outer flow, and furthermore causes the flow to accelerate due to entrainment. The displacement effect tends to increase the pressure felt at the base, whereas the entrainment acts to decrease the pressure [7]. The impact of the plume is dependent on the type of reattachment and can be small when reattachment occurs on the afterbody, sufficiently upstream of the nozzle exit [8]. On the other hand, strongly underexpanded jets have been shown to cause detachment of the shear layer from the afterbody, leading to a significantly larger recirculation region with stronger pressure fluctuations and an increase in base pressure [9].

Received 19 March 2018; revision received 15 September 2018; accepted for publication 24 September 2018; published online 11 December 2018.

[*] Ph.D. Student, Faculty of Aerospace Engineering, Aerodynamics Department, Kluyverweg 1; p.l.vangent@tudelft.nl.

[†] Graduate Student, Faculty of Aerospace Engineering, Aerodynamics Department, Kluyverweg 1.

[‡] Associate Professor, Faculty of Aerospace Engineering, Aerodynamics Department, Kluyverweg 1; b.w.vanoudheusden@tudelft.nl.

[§] Assistant Professor, Faculty of Aerospace Engineering, Aerodynamics Department, Kluyverweg 1; f.f.j.schrijer@tudelft.nl.

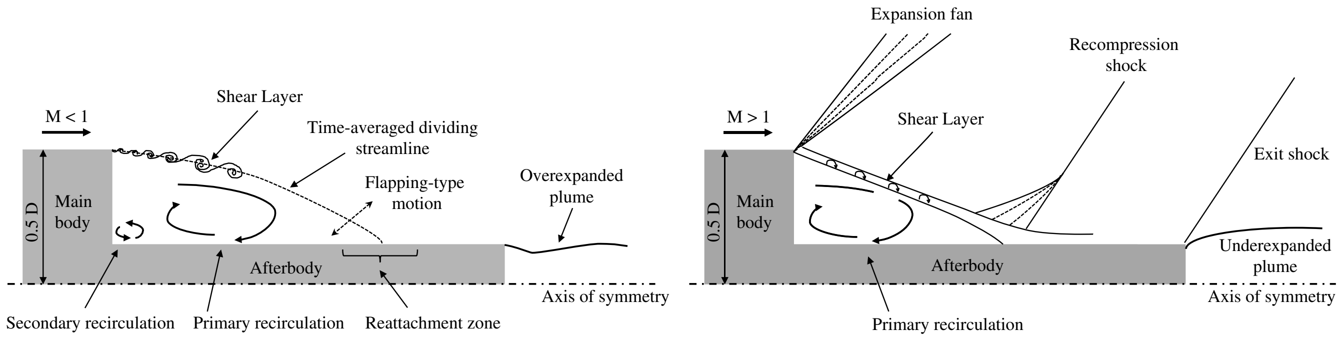

a) Subsonic base flow (based on Ref. [2]) **b) Supersonic base flow (based on Ref. [3])**

Fig. 1 Schematics of flow topology for base flows with an exhaust plume.

The base flow has been investigated in numerous experimental and numerical assessments that aimed to uncover the driving mechanisms of the flow dynamics and quantify the associated pressure loads. The majority of studies has considered freestream Mach numbers around 0.7, for which the critical mechanical loads typically occur (e.g., Refs. [8,10–13]). Others have addressed supersonic flow conditions (e.g., Refs. [14–17]). In view of the importance of quantifying (fluctuating) pressure loads to assist future design activities, many previous experimental assessments analyzed surface pressure data obtained with pressure transducers. The large-scale unsteady behavior of the flow may, however, be more conveniently characterized by means of global flow visualizations [18], including multipoint measurement techniques like particle image velocimetry (PIV) [1,12,13,19]. The latter has also been used to obtain measurements of the mean flowfield and Reynolds stress distributions [20], as well as to assess the impact of control devices [21,22]. A small number of studies used PIV in configurations with exhaust plumes [15,23,24]. However, despite the high relevance of quantifying pressure loads, the possibility of processing PIV velocity data to reconstruct pressure fields [25] has largely been left unexplored. In low-speed flows, the possibility of obtaining time-resolved PIV measurements allows the reconstruction of instantaneous pressure fields. In high-speed flows, this approach is, as of yet, not feasible, but the use of ensembles of uncorrelated PIV measurements still permits reconstruction of the mean pressure field [26]. This technique of deriving the pressure from the velocity data is particularly beneficial when the model geometry imposes spatial limitations for the installation of surface pressure taps or sensors, as is the case for a model equipped with a nozzle to generate an exhaust plume.

In view of the preceding, the particular focus of the present study is to assess the impact of an exhaust plume and of nozzle length on subsonic and supersonic axisymmetric base flows by characterizing the overall flow topology and pressure distribution. Ensembles of velocity fields are obtained by planar two-component PIV and processed to produce the spatial flow organization, which is expressed in terms of the mean velocity, mean pressure, turbulent kinetic energy, and the occurrence of reversed flow and mean pressure.

II. Experimental Arrangements

A. Flow Configuration and Model

The experiments were performed in the transonic-supersonic wind tunnel (TST-27) of the high-speed aerodynamics laboratories at Delft University of Technology. The facility has a test section with dimensions of 280 mm (width) × 270 mm (height). The wind tunnel was operated at nominal Mach numbers of 0.7 and 2.2. The transonic condition was selected because, in that regime, the maximum unsteady aerodynamic loads typically occurred. The Mach number of 2.2 was selected because, for this Mach number, the flow region of interest remained free from shocks reflected by the wind-tunnel wall.

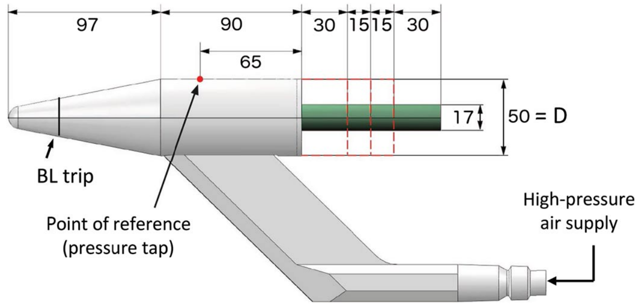

Fig. 2 Schematic of the model: side view (BL denotes boundary layer).

Due to the presence of the model and the nonnegligible blockage ratio of approximately 6%, we chose to use the conditions near the base of the main body as a reference. To quantify these conditions, the mean static pressure was conveniently measured via a pressure port located on the main body at 65 mm (1.3*D*) upstream of the base (see Fig. 2).

Table 1 lists the most relevant flow characteristics for the transonic and supersonic flow cases. Indicated ranges correspond to variations during a run and between different runs. Mach numbers and freestream velocities have been calculated using isentropic flow conditions. Due to the presence of a (curved) shock wave in front of the model, the total pressure is not constant. For the imposed deflection angles by the forebody and corresponding freestream Mach number, the variation in total pressure was estimated to remain below 3%.

A schematic of the model geometry is provided in Fig. 2. It has a conical nose with a semiapex angle of 11 deg and a nose radius of 7.5 mm. The cylindrical main body has a diameter *D* of 50 mm. The nose and main body have a total length of 187 mm. The afterbody contains a nozzle that allows generation of an exhaust plume of dry, unheated air that is supplied through tubing in the model support. Compressed air is delivered to the model from four 50 liter tanks, with each filled to a pressure of 300 bar. The model is equipped with a trip strip (0.15 mm diameter) applied at about 40% of the nose to ensure a fully developed, turbulent boundary layer. The thickness of the boundary layer on the model just upstream of the base is about 3 mm, as estimated based on PIV velocity data (see Sec. III.B). A more detailed characterization of the boundary layer over the model for Mach 0.7 was provided by Schrijer et al. [27].

Considering the internal geometry of the afterbody in more detail, it incorporates part of the settling chamber, the nozzle throat, and a

Table 1 Flow characteristics

Parameter	Symbol	Unit	Transonic	Supersonic
Reference Mach number	M_{ref}	——	0.76 ± 0.01	2.20 ± 0.01
Total pressure	$p_{0,\mathrm{ref}}$	bar	1.98 ± 0.01	2.41 ± 0.01
Reference static pressure	p_{ref}	bar	1.38 ± 0.01	0.23 ± 0.01
Total temperature	T_0	K	273 ± 3	277 ± 2
Reference velocity	U_{ref}	$\mathrm{m \cdot s^{-1}}$	236 ± 2	522 ± 2
Reynolds number	Re_D	——	1.5×10^6	0.8×10^6

Table 2 Jet flow characteristics

Parameter	Symbol	Unit	Transonic	Supersonic
Nozzle area ratio	A_e/A^*	——	6.8	6.8
Exit Mach number	M_e	——	3.5	3.5
Total pressure	p_0	bar	22 ± 2	27 ± 2
Exit static pressure	p_e	bar	0.29 ± 0.03	0.35 ± 0.03
Jet pressure ratio	p_e/p_∞	——	0.20 ± 0.02	1.57 ± 0.12
Total exit temperature	$T_{0,e}$	K	273	273

diverging section of the nozzle with a conical geometry (half-angle of 7.5 deg). The area ratio between the nozzle exit and the throat diameters (A_e/A^*) is 6.8. Variations in nozzle length L are achieved by sliding different collars over the nozzle. The present experiment considers four nozzle lengths: $L/D = 1.8, 1.2, 0.9$, and 0.6. The case of $L/D = 1.2$ represents a commonly used geometry that has been investigated in both the transonic flow regime [10,16,28] and the supersonic flow regime [17,29,30]. An original version of the model without adjustable nozzle length was used within the framework of the Future European Space Transportation Investigation Program (known as FESTIP) [31] and has been tested extensively in a series of experimental and numerical assessments (e.g., Refs. [12,32–34]).

The jet conditions are selected based on the exhaust conditions of the Ariane 5 Vulcain 2 engine, and they are shown in Table 2. The ranges correspond to variations observed during a run and between different runs. Although the exit Mach number of the Vulcain 2 is 4.56, the jet Mach number at the nozzle exit is limited to 3.5 in order to avoid condensation.

The jet total pressure p_0 was measured in the settling chamber compartment inside the model and was found to decrease by approximately 10% over the duration of each run (about 30 s) due to the control system of the compressed air supply. The exit pressure ratio showes that the jet was overexpanded ($p_e < p_{\mathrm{ref}}$) for $M_{\mathrm{ref}} = 0.76$ and underexpanded ($p_e > p_{\mathrm{ref}}$) for $M_{\mathrm{ref}} = 2.2$. The compressed air that was fed to the model was stored at an ambient temperature of about 288 K. From previous measurements in which the velocity in the plume exit was measured by PIV [34], it is known that the total jet temperature $T_{0,e}$ decreases by approximately 15 K due to heat losses in the piping to the model.

B. Similarity

At sufficiently high Reynolds numbers, the most important parameters to be duplicated in order to achieve a similar flow topology around a plume in the wind tunnel as in actual atmospheric flight are 1) the freestream Mach number, 2) the jet pressure ratio (p_e/p_∞), and 3) the jet velocity ratio (U_e/U_∞) [6,35].

The jet pressure ratio is especially important to achieve similarity in the shape of the jet boundary, and the displacement of the outer flow. The total pressure of the jet was therefore selected such that the jet pressure ratios in the experiments at Mach 0.76 and 2.2 [$(p_e/p_\infty)_{\mathrm{Exp.}} = 0.21$ and 1.57] were similar to the jet pressure ratios during the ascent of the Ariane 5/Vulcain 2 [$(p_e/p_\infty)_{\mathrm{Real.}} = 0.21$ and 1.53 [4,5]]. At similar jet pressure ratios, freestream Mach numbers, and ratios of specific heats in the freestream, the similarity in jet boundary shape is governed by $\gamma_e M_e (M_e^2 - 1)^{-1/2}$ [6]. Based on this parameter, the similarity of the jet boundary in the present experiments was as high as 91%.

The jet velocity ratio is important for achieving similarity in the growth rate of the shear layer and in the entrainment and acceleration of the outer flow. To allow rough indications of the similarity, first the velocity U_p and density ρ_p of the plume flow near the plume shear layer were estimated by considering isentropic expansion of the plume to the reference pressure of the outer flow. Using these results, velocity differences over the plume shear layer ($U_p - U_{\mathrm{ref}}$) in the present experiments at reference Mach numbers of 0.76 and 2.2 were estimated to be about 12 and 27 times smaller than in the real application, respectively; the shear layer growth rates at Mach 0.76 and 2.2 were estimated to be about 2.5 and 5 times smaller, respectively, by inserting the velocity ratios U_p/U_{ref} and the density ratios $\rho_p/\rho_{\mathrm{ref}}$ in the correlation proposed by Papamoschou and Roshko [36] while accounting for differences in compressibility effects; and the entrainment velocity, being proportionate to the shear layer thickness δ and the velocity difference over the shear layer ΔU [37], was estimated to be many times smaller than in the real application.

The aforementioned analysis underlines that, when using plumes of cold air, only a limited similarity with actual exhaust plumes can be achieved. This explains the use of gases different from air (e.g., Ref. [29]) and hot plumes [38–44], although such investigations are rare due to the practical challenges involved.

It should be noted that the jet pressure and velocity ratios can strictly only be used as a scaling parameters for flows around similar geometries. The precise shape of the plume is not so much defined by the ratio of the static jet pressure and the pressure in the freestream but, rather, by the ratio of the static jet pressure and local static pressure at the plume exit, which depends on the geometry. A similar argument holds for the jet flow velocity.

C. PIV Measurements

PIV measurements were performed in a streamwise-oriented plane. The field-of-view, sized $2.8D \times 1.0D$ (140×50 mm), encompassed part of the main body, the full nozzle, and part of the flow downstream of the nozzle. Figure 3 provides an overview of the PIV setup. The flow in the wind tunnel was seeded with titanium dioxide (TiO_2) particles of the Kemira P580 type. The particles had a primary crystal size of 30 nm (the actual particles form agglomerates of approximately 500 nm [45]), a nominal density of 150 $\mathrm{kg} \cdot \mathrm{m}^{-3}$, and a particle response time τ_p of 2.56 μs [46]. The particles were introduced in the tunnel by a seeding rake placed in the settling chamber, which was connected to a cyclone seeding generator. At $M_{\mathrm{ref}} = 0.76$, the distribution of particles was uniform in the field of view and the seeding intensity was relatively constant over different snapshots. For the case of $M_{\mathrm{ref}} = 2.2$, however, the seeding was observed to be intermittent; and strong variations in particle image density occurred throughout the field of view (see also Ref. [34]). The particles were illuminated by a double-cavity Nd:Yag laser of the Spectra-Physics Quanta Ray PIV-400 type. A 2-mm-thick laser light sheet was realized in the test section by means of an optical probe that was located downstream from the model.

Recording was performed by four LaVision Imager LX 2-megapixel cameras (pixel resolution of 1628×1236 pixels, and pixel size of 4.4×4.4 $\mu\mathrm{m}^2$) equipped with Nikon objectives of 105 mm operated at an aperture of $f/8.0$. The fields of view of the different cameras were placed next to each other in the streamwise direction with an overlap of about 4 mm. This arrangement resulted in a digital resolution of 30.3 $\mathrm{pixels} \cdot \mathrm{mm}^{-1}$ (optical magnification of 0.19). Recording was performed at 5 Hz in a double-frame mode. The time separation between two consecutive laser pulses was set at 2.5

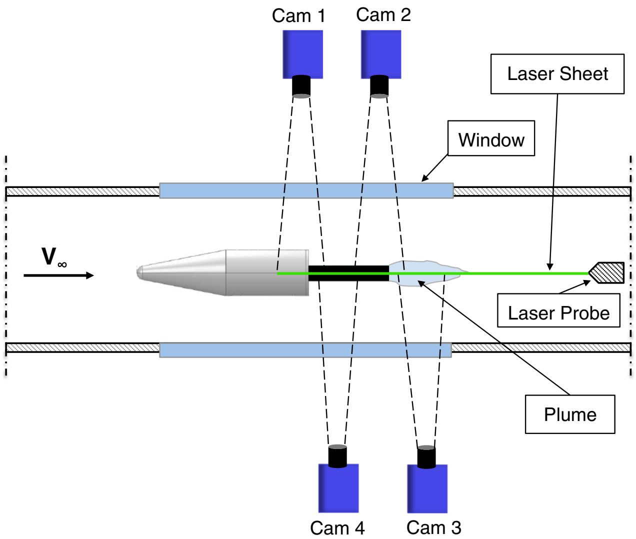

Fig. 3 Schematic of PIV setup: top view. (Cam denotes camera.)

and 1.0 μs for $M_{\mathrm{ref}} = 0.76$ and $M_{\mathrm{ref}} = 2.2$, respectively, leading to maximum particle displacements of about 25 and 23 pixels, respectively. The synchronization of all components and the acquisition of image data were ensured by an external timing unit controlled by LaVision DaVis software, version 8.1.2. For each configuration, at total of 500 snapshots were obtained, divided over four runs (125 snapshots per run). In total, 16 test configurations were considered (four nozzle lengths and two Mach numbers, with and without the jet). Based on a visual inspection of the recorded images and the final vector fields, 5–15% of the snapshots were found to suffer from insufficient seeding quality, depending on the case considered. These snapshots were removed before performing any subsequent analysis.

The contrast of the particle images was enhanced by subtracting the local minimum intensity in each run and the minimum intensity within 31×31 pixel-sized windows. The resulting intensity was normalized by a minimum–maximum filter with a kernel of 6×6 pixels. The velocity vector fields were obtained by a multigrid correlation procedure. Intermediate vector fields were processed by removing spurious vectors, which were identified by universal outlier detection [47], replacing them using linear interpolation and by a polynomial denoise filter. The final three iterations were performed using Gaussian-weighted elliptical interrogation windows (2:1) with a nominal window size of 48 pixels. As for the intermediate steps, spurious vectors were removed after the final step by universal outlier detection and replaced using linear interpolation. The overlap of the interrogation windows was 75%, resulting in a vector spacing of 0.40 mm (12 pixels). The instantaneous results were used to calculate the mean velocity fields and velocity fluctuation levels in a two-pass process. In the first pass, a preliminary standard deviation and preliminary mean value of the velocity were calculated for each point based on all snapshots in the ensemble. In the second pass, the standard deviation and mean value were recalculated using only instantaneous vectors that deviated less than three preliminary standard deviations from the preliminary mean.

The recorded images from the four cameras were analyzed separately. The aforementioned statistical results were combined and transferred to a common grid by linear interpolation. The final grid consisted of 420×137 points. PIV processing was performed using LaVision DaVis software, version 8.3.1.

Finally, the turbulent kinetic energy k was computed according to $k = (\sigma_u^2 + \sigma_v^2)/2$.

D. Pressure Calculation

The velocity results were used as input data to calculate the pressure fields according to a Reynolds-averaging approach [26,48–50], for which the Reynolds-averaged momentum equation was formulated as follows:

$$\frac{\partial\, ln\,(\langle p\rangle/p_{\mathrm{ref}})}{\partial x_i} = -\frac{1}{RT}\left(\langle u_j\rangle\frac{\partial\langle u_j\rangle}{\partial x_j} + \frac{\partial\langle u_i' u_j'\rangle}{\partial x_j}\right) \tag{1}$$

where u_i denotes the velocity component in direction x_i and "<>" indicates the averaging operator. Note that Eq. (1) does not contain temporal derivatives because these vanish in the averaging procedure. Terms associated with viscosity, the spatial gradient of the mean density, as well as density fluctuations only make a negligible contribution in the pressure determination, and are therefore omitted [26]. The density is eliminated from the original momentum equation with the gas law, whereas the temperature in Eq. (1) is related to the reference quantities and the local velocity magnitude by assuming the flow to be adiabatic [49,50]:

$$T = \frac{U_{\mathrm{ref}}^2 + ((\gamma-1)/2)M_{\mathrm{ref}}^2(U_{\mathrm{ref}}^2 - \langle U\rangle^2)}{\gamma R M_{\mathrm{ref}}^2} \tag{2}$$

The validity of assuming adiabatic flow for the purpose of pressure determination has been demonstrated for compressible flows with shocks [50] as well as for a transonic axisymmetric base flow [26].

Equation (1) was solved for pressure using a similar discretization method as in Ref. [51]. The pressure obtained from isentropic flow relations was used to formulate a Dirichlet boundary condition at the top of the domain for $-0.1 < x/D < 0.5$. This range was selected because of its availability and similarity in all flow cases considered. The validity of assuming isentropic flow at distances larger than two step heights from the afterbody was confirmed in Ref. [52]. To facilitate comparison of the different cases, the boundary condition was normalized with respect to the flow case with the longest nozzle ($L/D = 1.8$) without a plume. For a more detailed description of the procedure, the reader is referred to the work of van Gent et al. [26]. All pressure values were normalized according to $C_p = 2(p - p_{\mathrm{ref}})/(p_{\mathrm{ref}}\gamma M_{\mathrm{ref}}^2)$.

E. Measurement Accuracy and Pressure Validation

Errors in the PIV measurement may stem from various sources such as particle slip, system calibration, image noise, refraction of light due to density gradients, reflections of laser light, inhomogeneous seeding, the cross-correlation algorithm, and velocity gradients, as well as others [53–55]. These errors can be classified as systematic (or bias) errors or random errors. In general, based on inspection of the results, the velocity measurement errors can safely be assumed to be small as compared to the influence of changing the freestream Mach number from 0.76 to 2.2, significantly changing the model geometry or introducing an exhaust plume. Whereas it remains important to characterize the quality of the presented results, the measurement errors therefore do not constitute the dominant source of the observed differences between the flow cases considered.

In general, important sources of bias errors are the finite spatial resolution of the measurement and particle slip with respect to the flow. With the exception of flow regions with very high-velocity gradients such as in the shear layer in the direct vicinity of the step and near shocks, the errors associated with spatial resolution are estimated to be below $0.02U_{\mathrm{ref}}$, based on Ref. [52]. With regard to the particle slip, based on a flow time scale of $0.3D/1.3U_{\mathrm{ref}}$, with $0.3D$ being the step height and $1.3U_{\mathrm{ref}}$ the approximate maximum difference in mean streamwise velocity, the Stokes numbers are estimated to be 0.12 and 0.05 for $M_{\mathrm{ref}} = 0.7$ and $M_{\mathrm{ref}} = 2.2$, respectively, indicating errors below 1.5% [56]: again, except in flow regions with very high-velocity gradients.

The propagation of random velocity errors to statistical quantities was discussed in various works (e.g., Refs. [57] and [58]). An indicative estimate of the uncertainty in mean velocity due to instantaneous velocity random errors was obtained by assuming that the errors had a Gaussian distribution. Under this assumption and based on an ensemble size N of 500 images, the statistical convergence uncertainty in the mean velocity was estimated to be $N^{-1/2} = 4.5\%$ of the standard deviation of the measured velocity fluctuations, which translated to a maximum uncertainty of about 1% U_{ref}. Safely assuming that, in the flow regions of interest, the instantaneous velocity errors were small as compared to the velocity fluctuations in the flow, the uncertainty in the turbulent kinetic energy levels was estimated according to $U_k = ((\sigma_u^4 + \sigma_v^4)/2N)^{1/2}$ [58]. Noting that

$$U_k < (\sigma_u^2 + \sigma_v^2)/(2N)^{1/2} = k(2/N)^{1/2}$$

the maximum uncertainty was 6.3% (of the local level). Based on Ref. [50], the impact of random velocity errors on the value of the pressure coefficient C_p was estimated to be equal to twice the relative error in the absolute mean velocity.

The procedure for calculating pressure fields was validated for the present arrangements using earlier experiments on an axisymmetric base flow [26]. In those experiments, the model was supported by a rear-mounted sting that also acted as afterbody and that contained pressure sensors for a direct comparison with the PIV-based pressure results. The original validation considered tomographic PIV measurements that provided full volumetric velocity information. For the purpose of the present study, the validation has been extended to the use of planar two-component PIV and supersonic flow conditions (in that case, the experiments had been performed for a

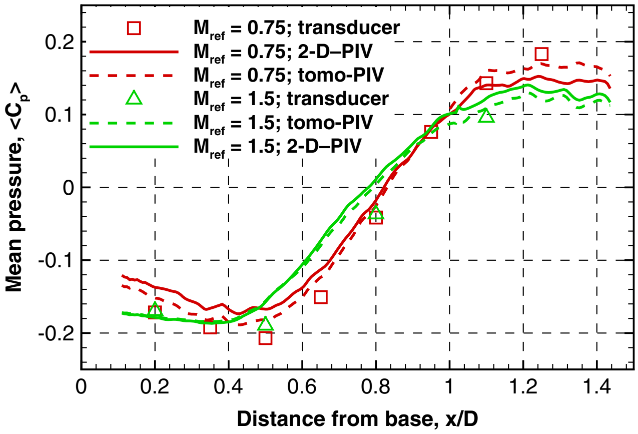

Fig. 4 Pressure on a base flow afterbody. (2-D denotes two-dimensional, and tomo denotes tomographic.)

Mach number of 1.5). The results of this additional assessment are presented in Fig. 4, which shows a comparison of PIV-based pressure and reference pressure measurements on the afterbody for reference Mach numbers of 0.75 and 1.5. The figure shows a good agreement between the two methods and confirms the suitability of planar, two-component PIV-based pressure determination.

III. Qualitative Flow Visualization and Incoming Boundary-Layer Profile

Before discussing the PIV results for the flow region near the base, a qualitative visualization of the complete flow around the model is given by means of schlieren visualization (Sec. III.A). In addition, specific attention is given to the boundary-layer velocity profiles upstream of the base to verify their similarity for the different flow cases (Sec. III.B).

A. Schlieren Visualization

Figure 5 shows schlieren visualizations for the transonic and supersonic flow cases with the shortest and the longest nozzles with the exhaust jet. Labels indicate 1) nose shock; 2) Mach wave from tripping wire; 3) expansion; 4) reflections; 5) Mach waves from pressure holes; 6) expansion over base; 7) shear layer; 8) recompression shock; 9) expansion of plume; 10) plume shear layer; 11) barrel shock; and 12) exit shock.

The two transonic cases on the left clearly show the growth of a shear layer from the base and an overexpanded jet at the nozzle exit. The shock wave at the nozzle exit seems to emanate from the interior of the nozzle and not from the nozzle tips. This suggests separation of the jet in the nozzle interior, which is a feature that conical nozzles are known to be particularly sensitive to.

Due to increased compressibility effects, the supersonic flow cases (right column) show more distinct features: a shock (point 1) emanating from the nose of the model due to displacement of the flow and, subsequently, an expansion fan (point 3) as the flow turns back in the horizontal direction. In addition, the figures show the Mach waves formed by the boundary layer trip (point 2) and the pressure taps (point 5). It can be verified that the reflections of the nose shock (point 4), the expansion fan, and the Mach waves from the wind tunnel wall do not intersect the area of interest downstream of the base. At the location of the step, an expansion fan can be observed (point 6) by which the flow turns toward the afterbody, as well as a shear layer (point 7) and a recompression shock (point 8) over which the flow turns back in the horizontal direction. Downstream of the

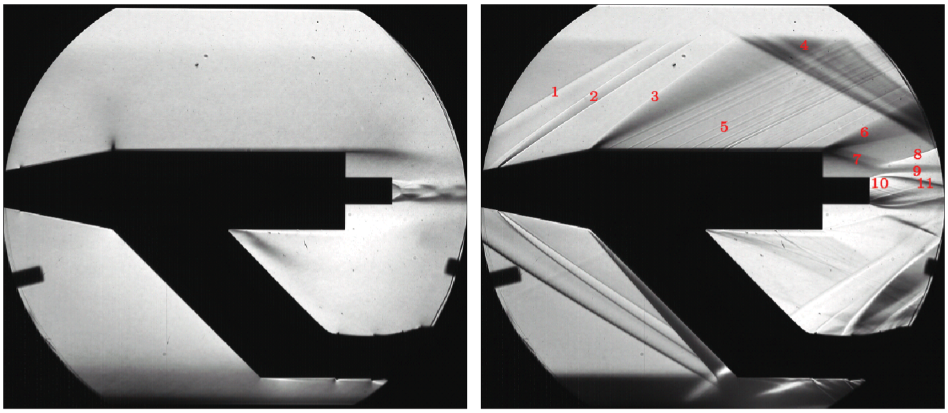

a) M_{ref} = 0.76; L/D=0.6

b) M_{ref} = 2.2; L/D = 0.6

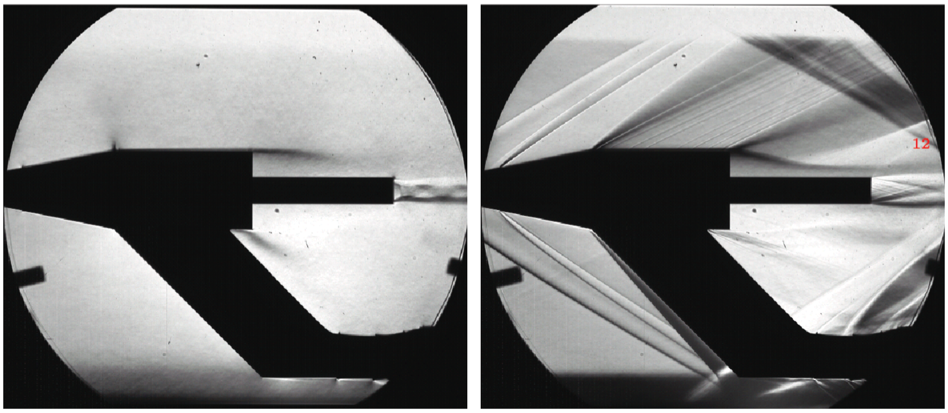

c) M_{ref} = 0.76; L/D=1.8

d) M_{ref} = 2.2; L/D=1.8

Fig. 5 Overview of schlieren visualizations.

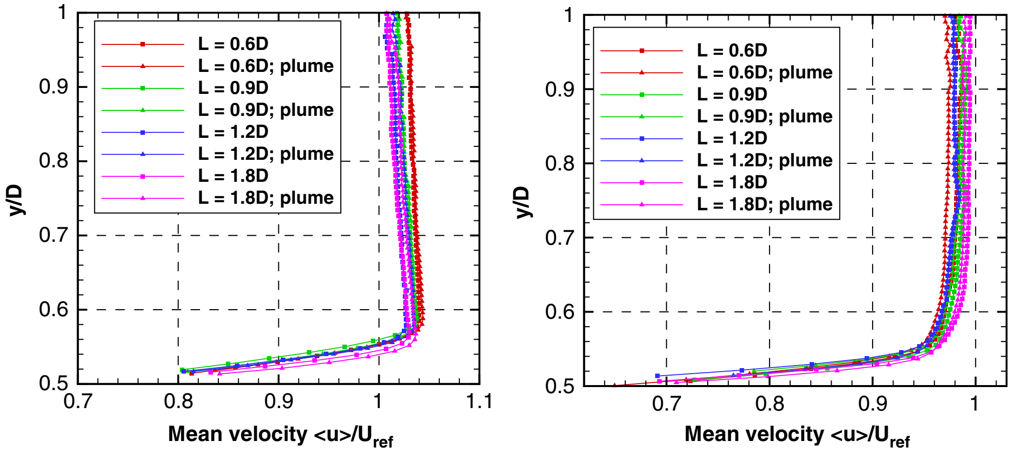

a) $M_{ref} = 0.76$ b) $M_{ref} = 2.2$

Fig. 6 Model boundary layer upstream of separation at $x/D = -0.1$.

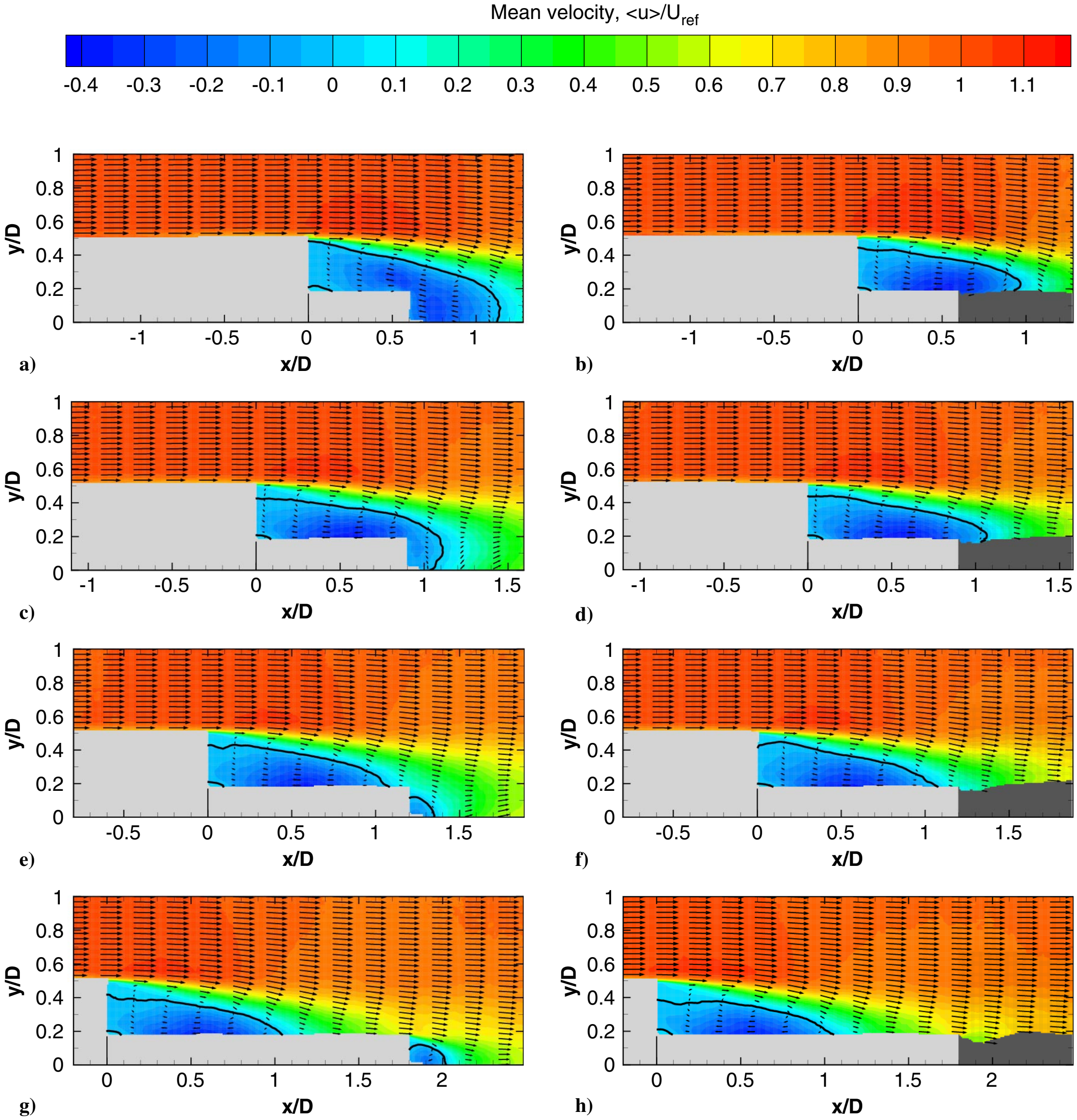

Fig. 7 Mean streamwise velocity for $M_{ref} = 0.76$ for increasing nozzle lengths (top to bottom): no plume (left), and with plume (right). Solid black lines indicate zero streamwise velocity.

recompression shock, a shear layer (point 9) can be observed that separates the plume and the outer flow. The underexpanded plume shows an expansion fan at the nozzle exit (point 10) and a barrel shock (point 11). Figure 5d shows that, for the longest nozzle length, a separate shock exists at the nozzle exit (point 12) due to the displacement of the flow by the plume.

Apart from the flow features mentioned previously, the figure shows that, due to the impact of the model support, the flow is not fully axisymmetric. This should be kept in mind when interpreting the results of this study.

B. Main Body Velocity Profile

To assess the flow over the main body upstream of the base and to verify that the flow upstream of the base flow interaction is similar for the different flow cases, Fig. 6 shows the mean streamwise velocity profile just upstream of the step, at $x/D = -0.1$. Due to limitations in the PIV spatial resolution and practical difficulties to view close to the model surface, the profile does not extend all the way to the model surface (see Ref. [27] for a more detailed characterization of the boundary layer over the model for Mach 0.7). The figures show that the inflow velocity varies by more than $0.01U_{\mathrm{ref}}$ between corresponding cases with and without the plume and by no more than $0.04U_{\mathrm{ref}}$ between cases with different nozzle lengths.

IV. Baseline Flow Organization

Before discussing the differences between different flow configurations, the following sections subsequently discuss the general organization of the mean velocity (Sec. IV.A), turbulent kinetic energy (Sec. IV.B), and mean pressure (Sec. IV.C).

A. Mean Velocity

Figures 7 and 8 show the mean velocity fields for $M_{\mathrm{ref}} = 0.76$ and $M_{\mathrm{ref}} = 2.2$, respectively. Colors indicate the value of the mean streamwise velocity component. Black contour lines indicate zero streamwise velocity. The left-hand-side figures correspond to flow cases without a plume, and the right-hand-side figures correspond to flow cases with a plume. The nozzle length increases from top to bottom, from $L/D = 0.6$ to 0.9, 1.2, and 1.8. The origin is located at the streamwise location of the trailing edge of the main body ($x/D = 0$) and at the centerline of the nozzle ($y/D = 0$). Bright gray

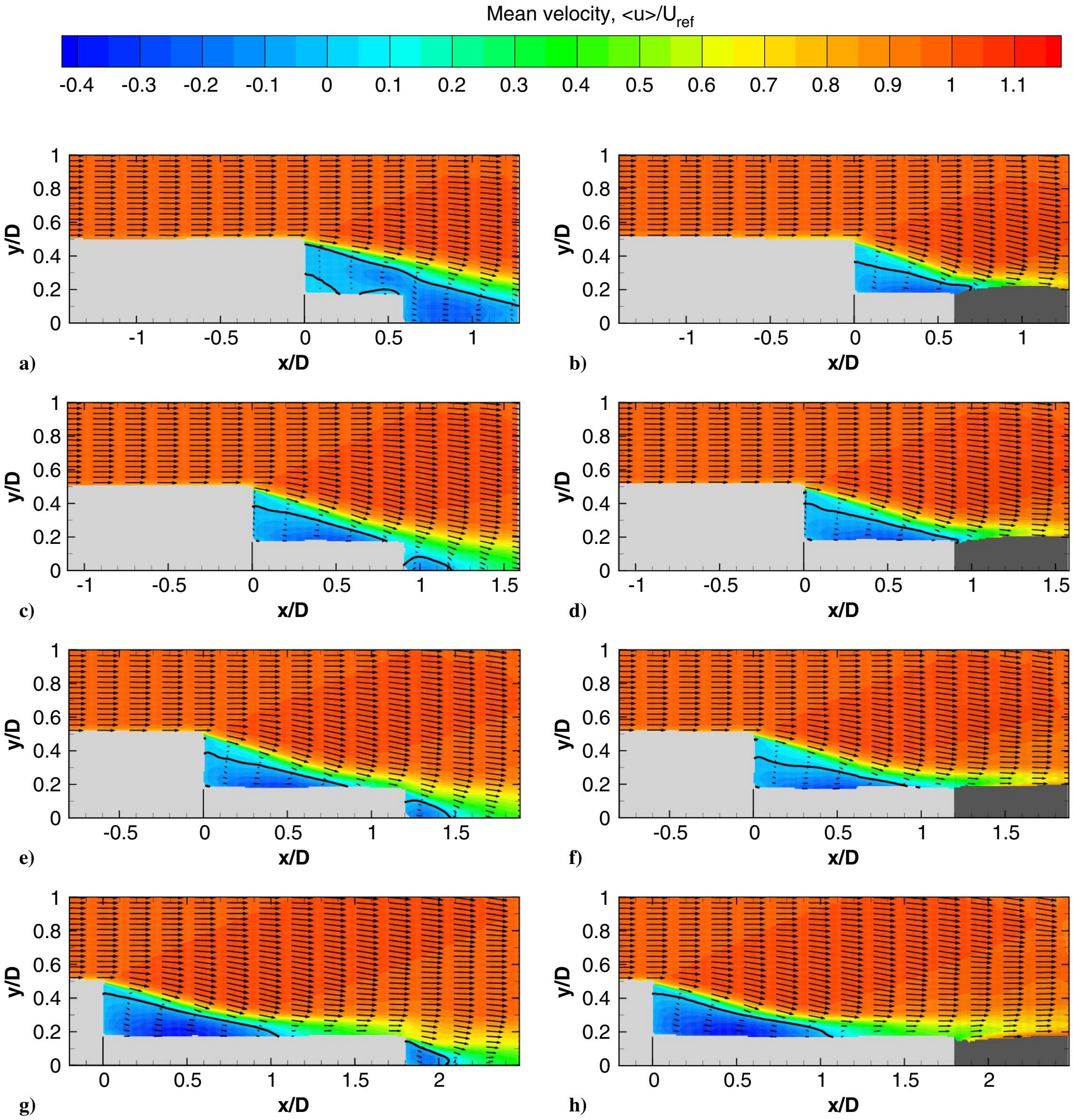

Fig. 8 Mean streamwise velocity for $M_{\mathrm{ref}} = 2.2$ for increasing nozzle lengths (top to bottom): no plume (left), and with plume (right). Solid black lines indicate zero streamwise velocity.

areas indicate the geometry of the model, whereas dark gray indicates the shape of the plume.

In general, the figures show a uniform incoming flow that deflects toward the nozzle as the flow moves past the step. A large-scale recirculation region with significant backflow ($u < 0$) is present downstream of the base. The outer flow and the recirculation region are separated by a shear layer that thickens toward reattachment. Depending on the configuration, the recirculation region extends to a stagnation point on the nozzle, to a point on the plume shear layer, or to a wake stagnation point downstream of the nozzle. In absence of an exhaust plume (left figures), there exists a recirculation downstream of the nozzle. As the nozzle remains open during the tests without plume, the recirculation in those cases likely extends to inside the model. At the junction of the base and nozzle at $x/D = 0$, the majority of cases show evidence of a small secondary recirculation region, which is formed due to separation of the backflow over the nozzle.

Compared to the transonic cases, the supersonic flow cases exhibit more pronounced deflections of the outer flow over the base, which is associated with a Prandtl–Meyer fan (compare Figs. 7 and 8). Furthermore, the supersonic cases show smaller recirculation regions and thinner shear layers. The latter is attributed to a reduced shear layer growth rate due to compressibility effects (e.g., Ref. [59]) in combination with a reduced unsteadiness of the shear layer, which is known to exhibit a pronounced flapping-type motion for transonic conditions [2,60].

B. Turbulent Kinetic Energy

The shear layer and reattachment region are associated with elevated levels of turbulent kinetic energy [$k = (\sigma_u^2 + \sigma_v^2)/2$], as shown by Figs. 9 and 10. Note the difference in scale between both figures. These elevated levels can be attributed to the presence of small-scale structures in the instantaneous flow organization as well as to the large-scale unsteadiness of the flow, which is known to encompass a flapping-type motion of the shear layer, vortex shedding, and growth/decay of the separated region [2,60]. These motions also account for part of the thickening of the shear layer toward reattachment, as observed in the time-averaged results. Typical turbulent kinetic energy levels above the shear layer and the model correspond to turbulence intensity levels in the range of 1–2% U_{ref}, which corresponds to the typical measurement uncertainty. More accurate hot-wire anemometry measurements performed in the same wind tunnel have been performed in Ref. [61] at a

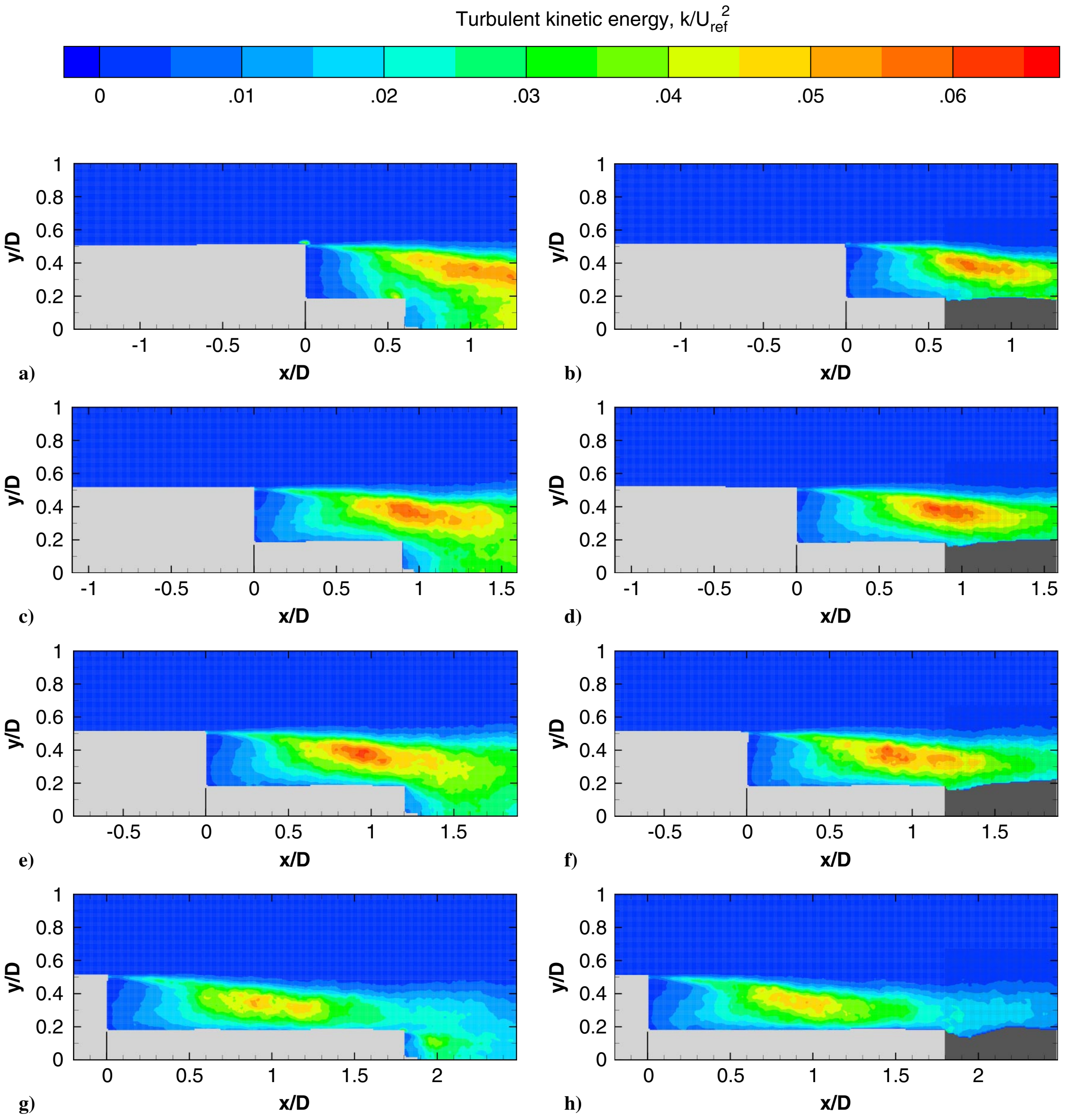

Fig. 9 **Turbulent kinetic energy (k/U_{ref}^2) for $M_{\mathrm{ref}} = 0.76$ for increasing nozzle lengths (top to bottom): no plume (left), and with plume (right).**

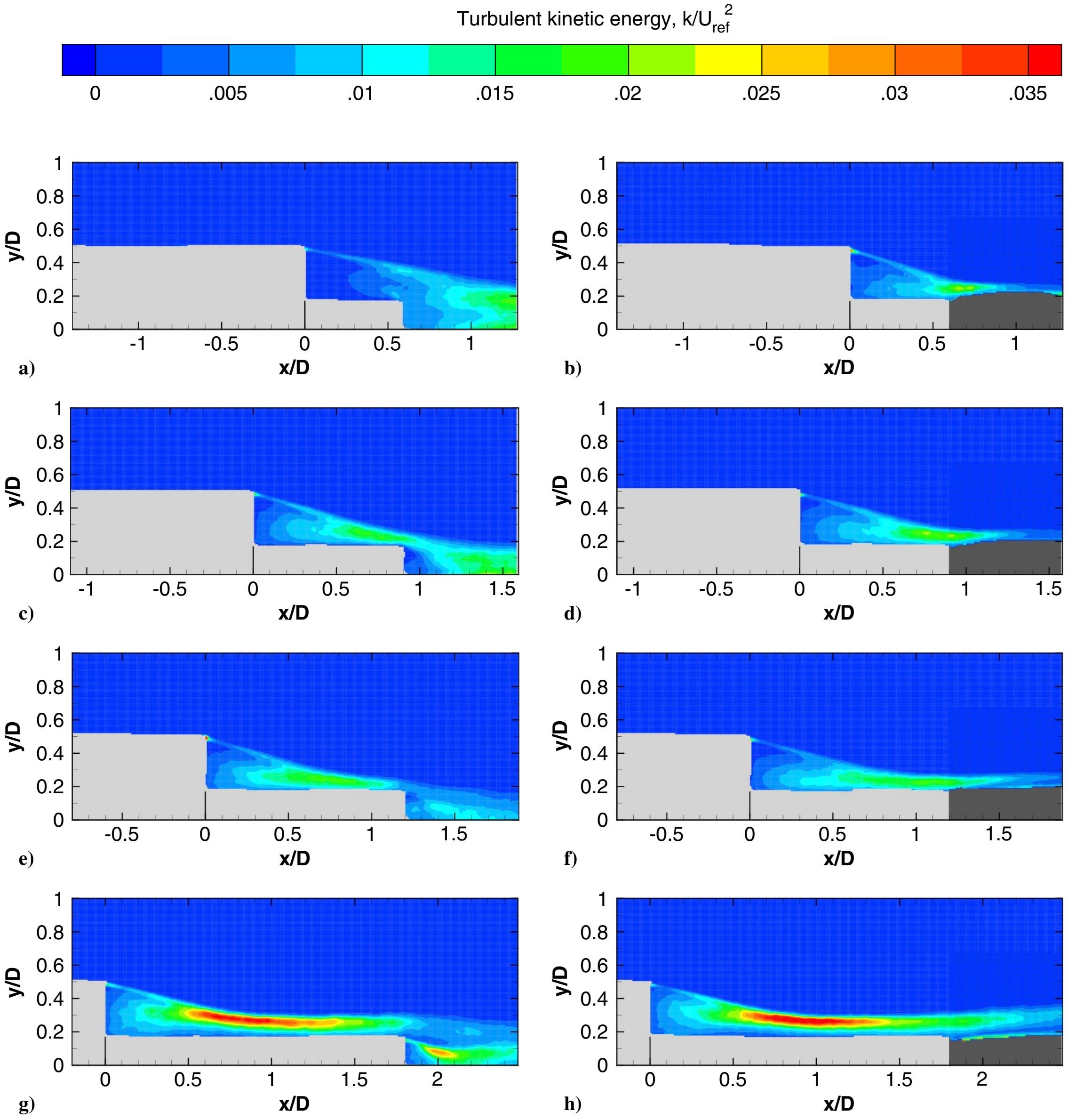

Fig. 10 Turbulent kinetic energy (k/U^2_{ref}) for $M_{\mathrm{ref}} = 2.2$ for increasing nozzle lengths (top to bottom): no plume (left), and with plume (right).

freestream Mach number of 1.7, in which a turbulence intensity of approximately 0.5% U_∞ was found.

Compared to the transonic flow cases, the supersonic flow cases exhibit much smaller relative turbulent kinetic energy levels. Furthermore, because the regions of highest levels coincide with the shear layer, they occur closer to the nozzle. The color scale of the figure does not reveal the signature of a recompression shock, which suggests that its position is relatively steady.

C. Mean Pressure

The mean pressure fields depicted in Figs. 11 and 12 show a low-pressure region downstream of the base. Further downstream, a high-pressure region is present, resulting from the recompression and realignment of the flow. Strong pressure gradients exist between the high- and low-pressure regions. The bottom figures show that, downstream of the location of maximum pressure, the pressure decreases again as the flow recovers from reattachment.

Large differences can be observed between the pressure fields for the transonic and supersonic flow cases. For $M_{\mathrm{ref}} = 0.76$, the isolines around the low-pressure region extend to upstream of the step. The supersonic cases, on the other hand, exhibit more oblique organizations of the pressure fields and high-pressure gradients at the locations of the expansion fan at the step and the recompression shock waves at reattachment, which agree with typical features of supersonic flow.

V. Impact of Nozzle Length and Plume

The impact of the nozzle and plume is assessed by considering the location of flow reattachment (Sec. V.A), the pressure in the base region (Sec. V.B), the shape of the plume (Sec. V.C), and the unsteadiness of the flow (Sec. V.D).

A. Location of Flow Reattachment

The mean reattachment length was determined as the streamwise location where the zero mean streamwise velocity contour (black lines in Figs. 7 and 8) intersects with the geometry or the plume. To facilitate Table 3 specifies the mean reattachment lengths for the different flow cases.

Focusing on $M_{\mathrm{ref}} = 0.76$, it can be observed that, for the two shortest nozzles (Figs. 7a–7d), the mean reattachment of the shear layer does not occur on the nozzle. In the other two cases with the longer nozzles (Figs. 7e–7h), mean reattachment occurs on the nozzle at about $x/D = 1.1$, which is similar to values reported in the literature for a freestream Mach number of 0.7 [10,16].

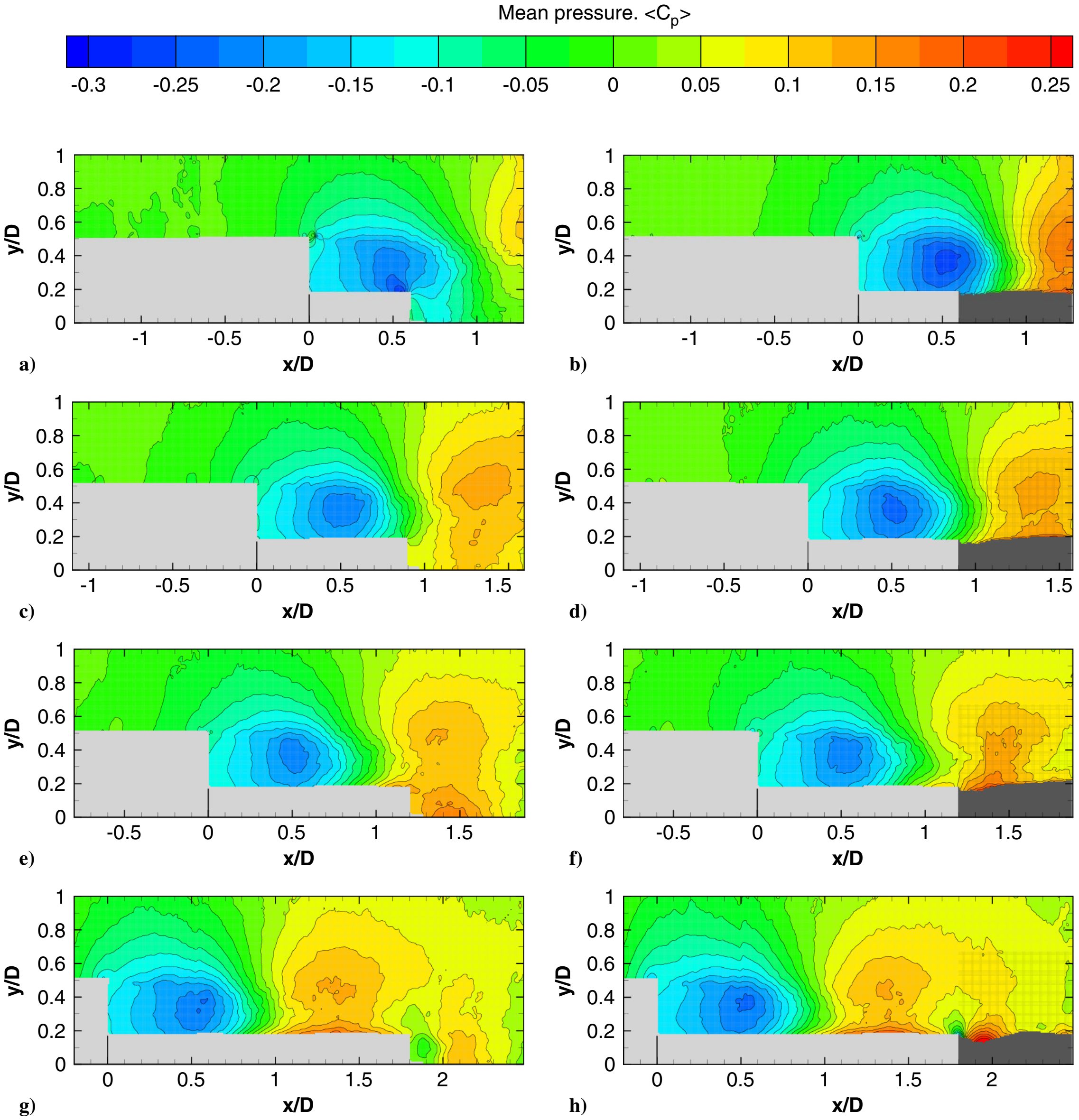

Fig. 11 Mean pressure for $M_{\mathrm{ref}} = 0.76$ for increasing nozzle lengths (top to bottom): no plume (left), and with plume (right).

For the supersonic flow cases, the mean reattachment length is generally smaller than under transonic conditions and increases with the nozzle length. This latter observation is speculatively attributed to the upstream propagation of the pressure rise associated with reattachment, which becomes more pronounced for the case of the longest nozzle (see also Fig. 12). For the cases without the plume, only for the shortest nozzle (Figs. 8a and 8b), mean reattachment does not occur on the nozzle. For the case of $L/D = 1.2$, the mean reattachment length of about 0.8D is similar to the lengths in the range of 0.8–0.7D reported in the literature for freestream Mach numbers of three and six [17,62].

With respect to the impact of the plume, at $M_{\mathrm{ref}} = 0.76$, the plume does not affect the reattachment length (compare first two columns in Table 3). It is noted that Wolf et al. [23] observed a shortening effect for low subsonic freestream velocities for an otherwise similar configuration. At $M_{\mathrm{ref}} = 2.2$, the plume leads to a elongation of the mean reattachment length (compare last two columns in Table 3). This effect becomes less pronounced for longer nozzles. Similar to before, the elongation of the separated region is speculatively attributed to the upstream propagation of the pressure rise associated with the displacement of the flow by the plume (see also Fig. 12).

The probability of reversed flow ($P(u < 0)$) for each location is determined as the share of the instantaneous snapshots for which reversed flow occurs (Figs. 13 and 14). Whereas the foregoing discussion considered the location of mean reattachment, the range of instantaneous reattachment locations is estimated from the reversed flow probability as the streamwise distance at $y/D = 0.2$ between $P(u < 0) \approx 0.9$ and $P(u < 0) \approx 0.1$.

Using this approach, it can be inferred from Fig. 13 that, at $M_{\mathrm{ref}} = 0.76$, for $L/D = 0.6$ reattachment always occurs downstream of the nozzle (fluidic reattachment); for $L/D = 0.9$ intermittently on and downstream of the nozzle (hybrid reattachment) and 1.2; and for $L/D = 1.8$ always on the nozzle (solid reattachment). Similarly, it is inferred from Fig. 13 that at $M_{\mathrm{ref}} = 2.2$, the reattachment is fluidic for $L/D = 0.6$, and it is solid for $L/D = 1.2$ and 1.8. $L/D = 0.9$ seems to be a case that is on the limit between hybrid and solid, depending on the presence of the plume.

B. Base Pressure

To assess the impact of the nozzle length and the plume on the overall pressure level in the base region, Table 4 lists the minimum pressure in the base region and Fig. 15 shows the pressure profile over the nozzle ($y/D = 0.2$). The results show that for the shortest nozzle, for which fluidic reattachment occurs, the plume leads to a drastic reorganization of the pressure field (see also Figs. 11a, 11b, 12a, and 12b). For the

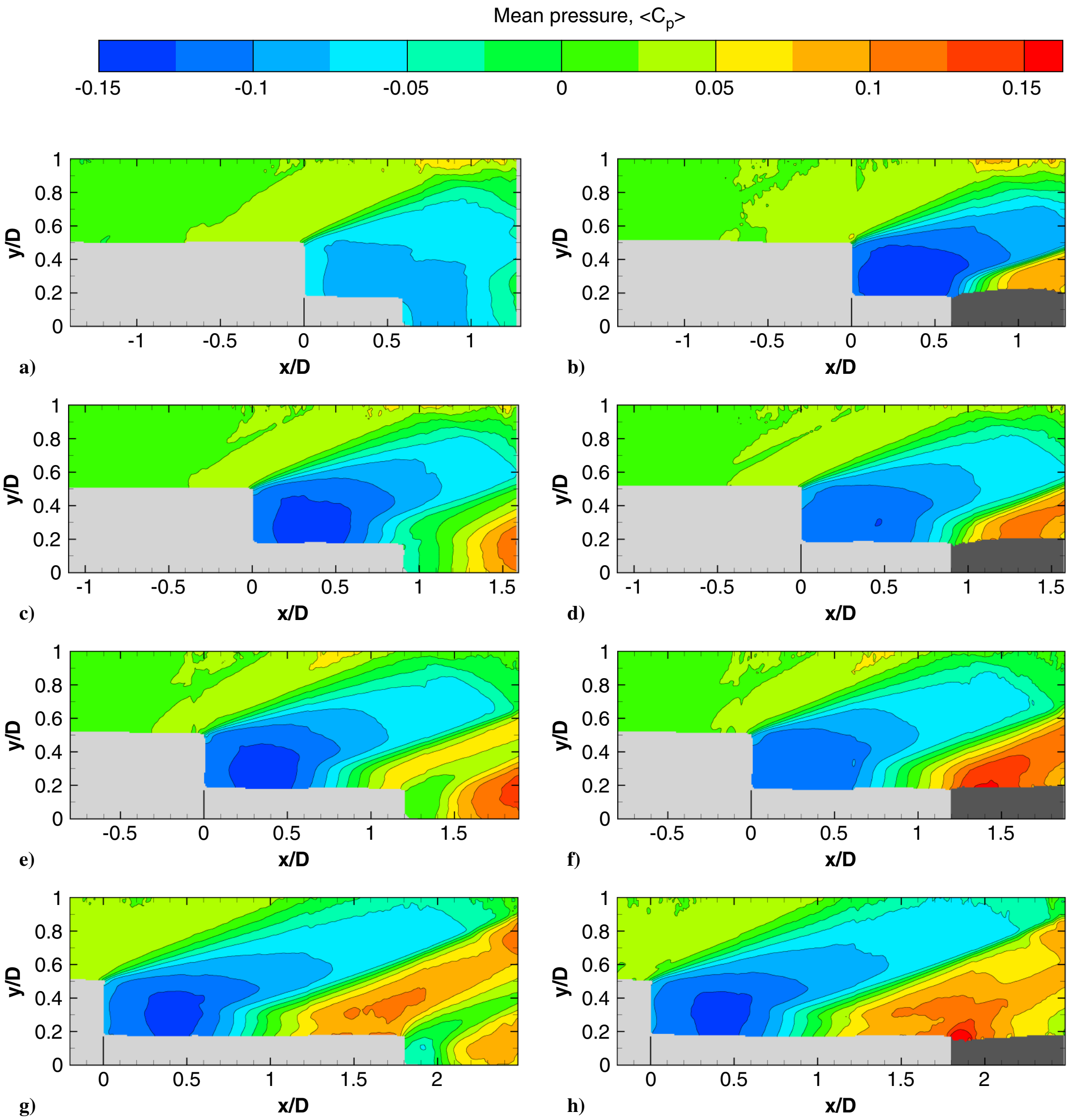

Fig. 12 **Mean pressure for $M_{\mathrm{ref}} = 2.2$ for increasing nozzle lengths (top to bottom): no plume (left), and with plume (right).**

longest nozzle, however, the impact of the plume on the pressure directly downstream of the base is very small or even negligible, which is in line with observations in Ref. [8]. For the two intermediate nozzle lengths for which the reattachment is hybrid or ”only just” solid, the overall pressure level downstream of the base decreases in the transonic flow cases (Figs. 11c–11f) and increases in the supersonic flow cases (Figs. 12c–12f). These trends agree with the literature [7,8,23,63]. The pressure decrease in the transonic flow regime can be attributed to the acceleration of the flow downstream of reattachment due to its entrainment in the plume shear layer. As discussed in Sec. II.B, this effect is much smaller in the present experiments than in the real application. The pressure increase in the supersonic flow regime can be attributed to displacement of the reattaching flow by the plume. In fact, both entrainment and displacement occur in both flow regimes. During the ascent of launchers, the plume becomes increasingly underexpanded, leading to a larger displacement.

Table 3 **Mean reattachment length (L_R/D)**

L/D	$M_{\mathrm{ref}} = 0.76$ no plume	$M_{\mathrm{ref}} = 0.76$ plume	$M_{\mathrm{ref}} = 2.2$ no plume	$M_{\mathrm{ref}} = 2.2$ plume
0.6	——	0.9	——	0.7
0.9	——	1.0	0.8	0.9
1.2	1.1	1.1	0.8	0.9
1.8	1.1	1.1	1.0	1.0

C. Nozzle Exit Conditions

Comparison of the mean pressure fields for flow cases (Figs. 11 and 12) shows that the location of the low-pressure region downstream of the base typically lies at $x/D \approx 0.50$ and $y/D \approx 0.35$, and that it is relatively invariant for the different flow cases. As the nozzle length increases, the nozzle therefore extends into the high-pressure region. The nozzle exit is then located in a flow region with higher pressure, which seems to result in more overexpanded plumes in the transonic flow cases and less underexpanded plumes in the supersonic flow cases. These differences in the state of the plume are confirmed by means of schlieren visualization.

D. Flow Unsteadiness

The difference in unsteady flow behavior for the different cases is assessed on the basis of the turbulence kinetic energy shown in Figs. 9 and 10. The first of these figures shows that, for $M_{\mathrm{ref}} = 0.76$, the greatest turbulence levels occur for $L/D = 0.9$ and 1.2 (Figs. 9c–9f), which may likely be the result of increased flow unsteadiness due to the intermittent occurrence of reattachment on the nozzle and on the downstream flow (hybrid reattachment). The longest nozzle for

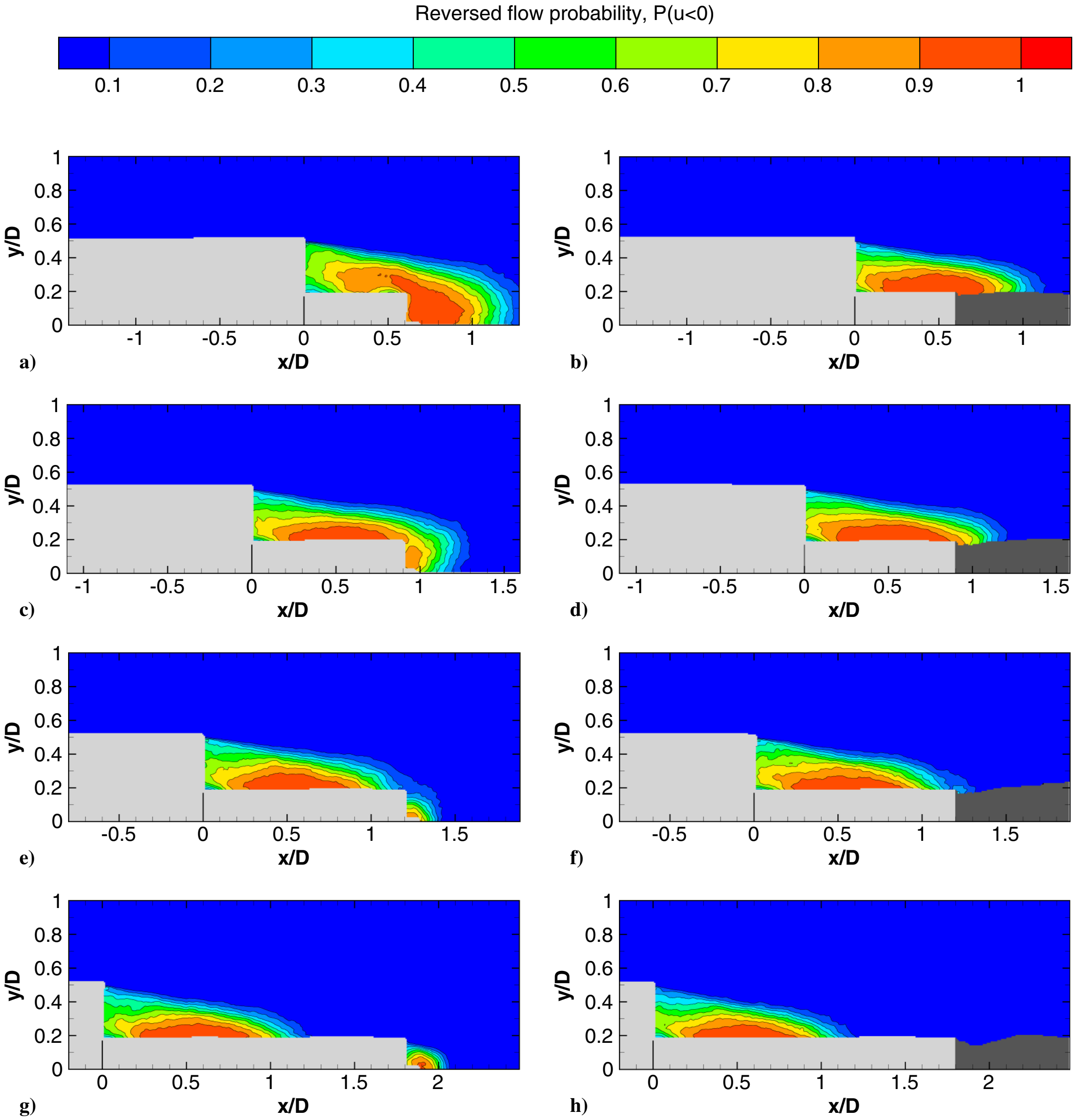

Fig. 13 **Probability of reversed flow ($(P(u < 0))$) for $M_{\text{ref}} = 0.76$ for increasing nozzle lengths (top to bottom): no plume (left), and with plume (right).**

which solid reattachment occurs, exhibits the lowest turbulent kinetic energy levels.

For $M_{\text{ref}} = 2.2$, it is remarkable that the flow cases with the three shortest nozzles (Figs. 9a–9f) all have similar maximum turbulence kinetic energy levels, whereas the levels for the longest nozzle (Figs. 9g–9h) are about twice as high. These higher levels are of similar magnitude as the maxima obtained for the validation experiment, with a long afterbody described in Sec. II.E, as well as the maximum of $0.044U_\infty^2$ reported by Herrin and Dutton [64] based on laser Doppler velocimetry measurements in the wake of a blunt base. It is noted that, apart from actual physical variations in the degree of flow unsteadiness, the fact that the observed turbulence levels for the shorter nozzles are relatively low could be the result of a more pronounced underestimation of turbulent kinetic levels due to limitations in spatial resolution or due to a different distribution of fluctuations over the in-plane and out-of-plane velocity components.

With regard to the impact of the plume, for $M_{\text{ref}} = 0.76$, the presence of the plume does not seem to greatly affect the organization of turbulence kinetic energy or the maximum levels, except for the shortest nozzle (Figs. 9a and 9b). This also becomes apparent from Table 5, which lists the maximum turbulence kinetic energy observed in the shear layer. The observation that the presence of a plume is not accompanied by higher fluctuation levels is consistent with the results reported in the literature [8,23]. For $M_{\text{ref}} = 2.2$, the region with elevated turbulence levels extends farther downstream in the presence of a plume, and may contain higher maxima (see also Table 5).

Table 4 **Minimum pressure in base region $C_{p,\min}$**

L/D	$M_{\text{ref}} = 0.76$ no plume	$M_{\text{ref}} = 0.76$ plume	$M_{\text{ref}} = 2.2$ no plume	$M_{\text{ref}} = 2.2$ plume
0.6	−0.28	−0.26	−0.09	−0.15
0.9	−0.21	−0.23	−0.14	−0.13
1.2	−0.21	−0.22	−0.14	−0.12
1.8	−0.23	−0.23	−0.14	−0.14

Table 5 **Maximum turbulent kinetic energy (k/U_{ref}^2) in the shear layer**

L/D	$M_{\text{ref}} = 0.76$ no plume	$M_{\text{ref}} = 0.76$ plume	$M_{\text{ref}} = 2.2$ no plume	$M_{\text{ref}} = 2.2$ plume
0.6	0.057	0.061	0.018	0.022
0.9	0.061	0.064	0.018	0.021
1.2	0.062	0.061	0.020	0.019
1.8	0.052	0.051	0.038	0.043

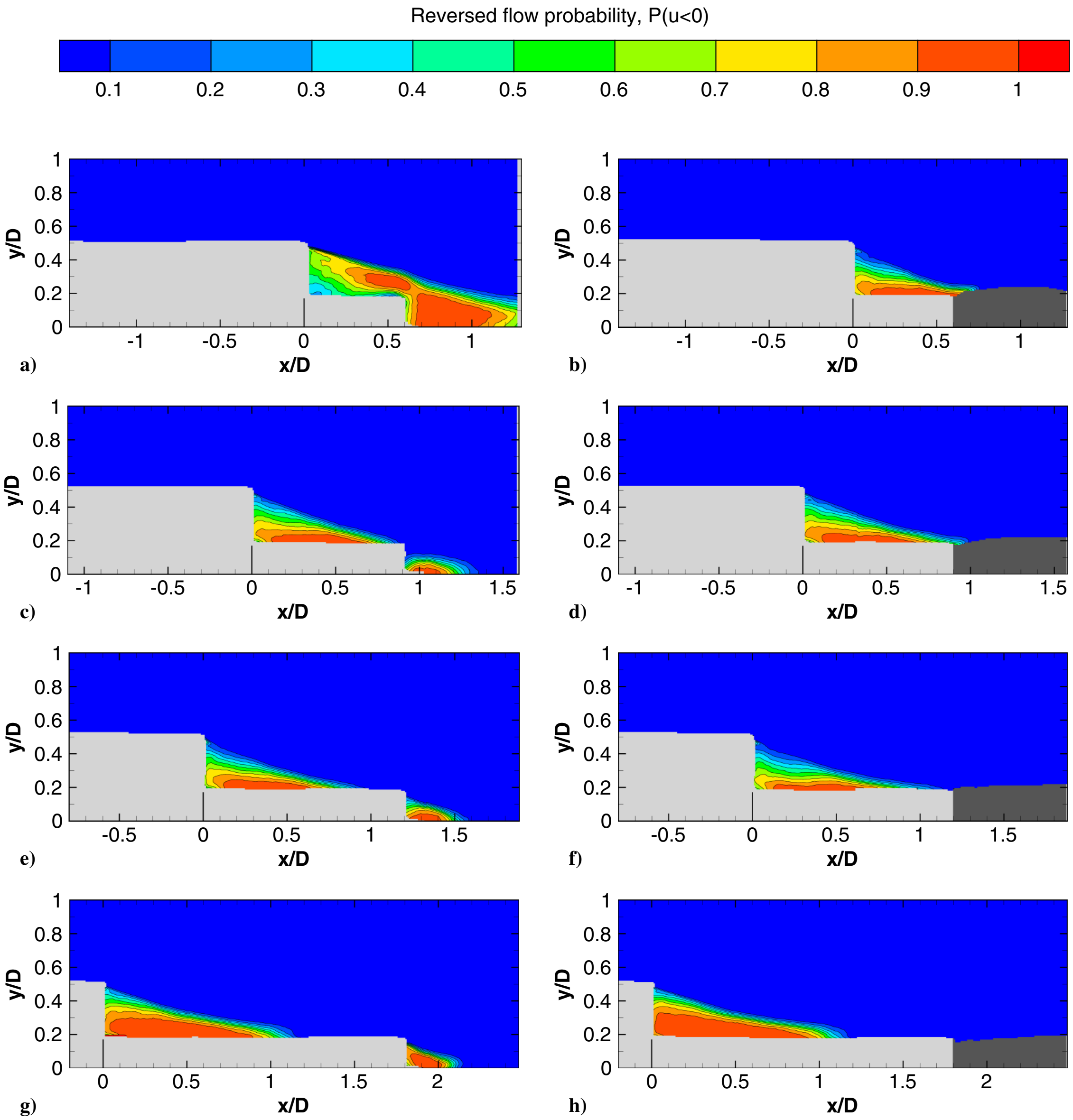

Fig. 14 **Probability of reversed flow ($P(u < 0)$) for $M_{\mathrm{ref}} = 2.2$ for increasing nozzle lengths (top to bottom): no plume (left), and with plume (right).**

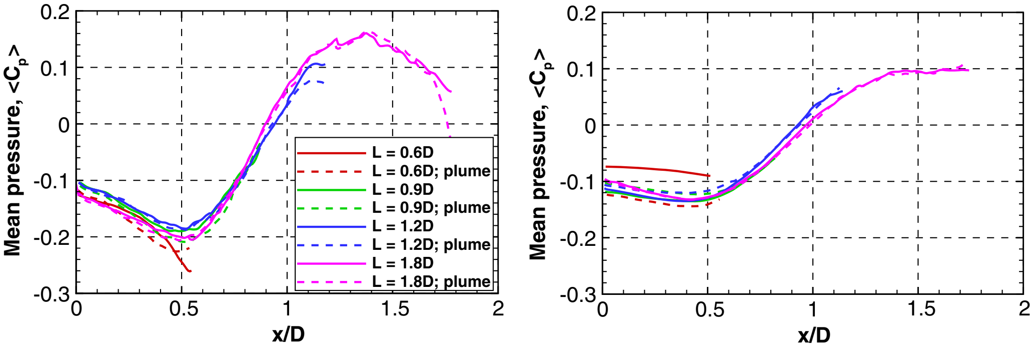

a) $M_{ref} = 0.76$

b) $M_{ref} = 2.2$

Fig. 15 **Mean pressure over the nozzle.**

VI. Conclusions

An experimental assessment has been carried out to study the effects of an exhaust plume and nozzle length on transonic and supersonic axisymmetric base flows. A generic geometry was considered with four different nozzle lengths ($L/D = 0.6$, 0.9, 1.2, and 1.8). The impact of the exhaust plume was simulated by means of a cold jet. The total pressure of the jet was set to achieve approximate similarity with the ascent of the Ariane 5, such that the jet was overexpanded at Mach 0.76 and underexpanded at Mach 2.2. The use of different nozzle lengths resulted in flow cases in which the shear layer impinged on the model (solid reattachment), on the flow downstream of the model (fluidic reattachment), or intermittently on the model and on the flow (hybrid reattachment).

At $M_{\mathrm{ref}} = 0.76$, no effect of the plume on the reattachment length could be observed. At $M_{\mathrm{ref}} = 2.2$, however, the introduction of the plume was accompanied by a longer mean reattachment length. This effect was found to become less pronounced for longer nozzles. The elongation of the separated region was speculatively attributed to the upstream propagation of the pressure rise associated with the displacement of the flow by the plume.

For the shortest nozzle, for which fluidic reattachment occurred, the plume led to a drastic reorganization of the pressure field. For the longest nozzle, the impact of the plume on the pressure directly downstream of the base was very small or even negligible. For the two intermediate nozzle lengths for which the reattachment was hybrid or just solid, the overall pressure level downstream of the base decreased in the transonic flow cases and increased in the supersonic flow cases. These observations could be explained by the effects of entrainment and displacement, respectively [7,8,23,63].

Comparisons of flow cases with a long nozzle without a plume and flow cases with a short nozzle but with a plume suggest that the presence of the plume cannot accurately be modeled by replacing the plume with a solid geometry. This is because:

1) It is difficult to a priori know the shape of the plume.

2) Whereas the flow will decelerate toward the surface of a solid, in the presence of a plume, the outer flow accelerates due to entrainment.

From observations of the transonic flow cases, hybrid reattachment was associated with increased turbulent kinetic energy levels and solid reattachment with the lowest, thus indicating a stabilizing effect on the flow, which was also observed in previous publications [8,23]. In contrast, the supersonic flow case with the longest nozzle, for which solid reattachment occurred, showed a remarkably strong increase in the occurrence of reversed flow and in-plane turbulent kinetic energy.

An increase in nozzle length was found to correspond to a higher local pressure near the nozzle exit, which seemed to result in more overexpanded plumes in the transonic flow cases and less underexpanded plumes in the supersonic flow cases, with otherwise equal internal nozzle geometries and freestream pressures. This effect was likely confined to the vicinity of the nozzle exit, where the impact of flow separation from the base was felt. Even so, the difference between the exit pressure and local ambient pressure is of key importance to the performance of a nozzle in terms of the amount of thrust generated. This study therefore highlighted the need of considering, during vehicle design, that a longer nozzle in which the plume expands further, not only corresponds to a lower exit pressure, but also to a different ambient pressure near the nozzle exit.

Acknowledgments

This work has been supported by the European Union's Seventh Framework Programme for research, development, and demonstration under grant agreement no. 605151, pertaining to the NIOPLEX (which stands for non-intrusive optical pressure and loads extraction for aerodynamic analysis) project.

References

[1] Schrijer, F., Sciacchitano, A., Scarano, F., Hannemann, K., Pallegoix, J., Maseland, J., and Schwane, R., "Experimental Investigation of Base Flow Buffeting on the Ariane 5 Launcher Using High Speed PIV," *7th European Symposium on Aerothermodynamics*, ESA Communications, Noordwijk, The Netherlands, 2011.

[2] Driver, D. M., Seegmiller, H. L., and Marvin, J. G., "Time-Dependent Behavior of a Reattaching Shear Layer," *AIAA Journal*, Vol. 25, No. 7, 1987, pp. 914–919.
doi:10.2514/3.9722

[3] Loth, E., Kailasanath, K., and Loehner, R., "Supersonic Flow over an Axisymmetric Backward-Facing Step," *Journal of Spacecraft and Rockets*, Vol. 29, No. 3, 1992, pp. 352–359.
doi:10.2514/3.26358

[4] "Ariane 5–VA226–Launch Profile," SpaceFlight101.com (online database), http://spaceflight101.com/ariane-5-va226/ariane-5-va226-launch-profile/ [retrieved 04 Nov. 2018].

[5] *Ariane 5 User's Manual*, No. 5, Rev. 2, Ariane Space, 2016.

[6] Pindzola, M., *Jet Simulation in Ground Test Facilities*, Vol. 79, NATO, Advisory Group for Aeronautical Research and Development, Paris, 1963, pp. 13–14.

[7] Bergman, D., "Effects of Engine Exhaust Flow on Boattail Drag," Journal of Aircraft, Vol. 8, No. 6, 1971, pp. 434–439; also *8th Aerospace Sciences Meeting*, AIAA Paper 1970-0132, 1970.
doi:10.2514/6.1970-132

[8] Deprés, D., Reijasse, P., and Dussauge, J. P., "Analysis of Unsteadiness in Afterbody Transonic Flows," *AIAA Journal*, Vol. 42, No. 12, 2004, pp. 2541–2550.
doi:10.2514/1.7000

[9] Statnikov, V., Sayadi, T., Meinke, M., Schmid, P., and Schröder, W., "Analysis of Pressure Perturbation Sources on a Generic Space Launcher After-Body in Supersonic Flow Using Zonal Turbulence Modeling and Dynamic Mode Decomposition," *Physics of Fluids*, Vol. 27, No. 1, 2015, Paper 016103.
doi:10.1063/1.4906219

[10] Weiss, P.-E., Deck, S., Robinet, J.-C., and Sagaut, P., "On the Dynamics of Axisymmetric Turbulent Separating/Reattaching Flows," *Physics of Fluids*, Vol. 21, No. 7, 2009, Paper 075103.
doi:10.1063/1.3177352

[11] Hannemann, K., Lüdeke, H., and Pallegoix, J., "Launch Vehicle Base Buffeting-Recent Experimental and Numerical Investigations," *Proceedings of the 7th European Symposium on Aerothermodynamics*, ESA SP-692, Brugge, Belgium, May 2011, p. 102.

[12] Schrijer, F. F. J., Sciacchitano, A., and Scarano, F., "Spatio-Temporal and Modal Analysis of Unsteady Fluctuations in a High-Subsonic Base Flow," *Physics of Fluids*, Vol. 26, No. 8, 2014, Paper 086101.
doi:10.1063/1.4891257

[13] Scharnowski, S., Statnikov, V., Meinke, M., Schröder, W., and Kähler, C. J., "Combined Experimental and Numerical Investigation of a Transonic Space Launcher Wake," *Progress in Flight Physics*, Vol. 7, edited by D. Knight, I. Lipatov, and P. Reijasse, EDP Sciences, Les Ulis, France, 2015, pp. 311–328.
doi:10.1051/eucass/201507311.

[14] Janssen, J. R., and Dutton, J. C., "Time-Series Analysis of Supersonic Base-Pressure Fluctuations," *AIAA Journal*, Vol. 42, No. 3, 2004, pp. 605–613.
doi:10.2514/1.4071

[15] Scarano, F., van Oudheusden, B. W., Bannink, W., and Bsibsi, M., "Experimental Investigation of Supersonic Base Flow Plume Interaction by Means of Particle Image Velocimetry," *Proceedings of the Fifth European Symposium on Aerothermodynamics for Space Vehicles (ESA SP-563)*, edited by D. Danesy, Cologne, Germany, 2004, p. 601.

[16] Deck, S., and Thorigny, P., "Unsteadiness of an Axisymmetric Separating-Reattaching Flow: Numerical Investigation," *Physics of Fluids*, Vol. 19, No. 6, 2007, Paper 065103.
doi:10.1063/1.2734996

[17] Statnikov, V., Stephan, S., Pausch, K., Meinke, M., Radespiel, R., and Schröder, W., "Experimental and Numerical Investigations of the Turbulent Wake Flow of a Generic Space Launcher at $M = 3$ and $M = 6$," *CEAS Space Journal*, Vol. 8, No. 2, 2016, pp. 101–116.
doi:10.1007/s12567-016-0112-x

[18] Mueller, T. J., "The Role of Flow Visualization in the Study of Afterbody and Base Flows," *Experiments in Fluids*, Vol. 3, No. 2, 1985, pp. 61–70.
doi:10.1007/BF00276711

[19] Bitter, M., Scharnowski, S., Hain, R., and Kähler, C. J., "High-Repetition-Rate PIV Investigations on a Generic Rocket Model in Sub- and Supersonic Flows," *Experiments in Fluids*, Vol. 50, No. 4, 2011, pp. 1019–1030.
doi:10.1007/s00348-010-0988-8

[20] Scharnowski, S., and Kähler, C. J., "Investigation of a Transonic Separating/Reattaching Shear Layer by Means of PIV," *Theoretical and Applied Mechanics Letters*, Vol. 5, No. 1, 2015, pp. 30–34.
doi:10.1016/j.taml.2014.12.002

[21] Schrijer, F. F. J., Sciacchitano, A., and Scarano, F., "Experimental Investigation of Flow Control Devices for the Reduction of Transonic Buffeting on Rocket Afterbodies," *15th International Symposium on Applications of Laser Techniques to Fluid Mechanics*, Lisbon, July 2010.

[22] Scharnowski, S., Bolgar, I., and Kähler, C., "Control of the Recirculation Region of a Transonic Backward-Facing Step Flow Using Circular Lobes," *9th International Symposium on Turbulence and Shear Flow Phenomena (TSGP-9)*, Melbourne, Australia, June–July 2015.

[23] Wolf, C., Klei, C., Buffo, R., Hörnschemeyer, R., and Stumpf, E., "Comparison of Rocket Near-Wakes with and Without Nozzle Simulation in Subsonic Freestream Conditions," *42nd AIAA Fluid*

Dynamics Conference and Exhibit, AIAA Paper 2012-3019, 2012. doi:10.2514/6.2012-3019

[24] Bolgar, I., Scharnowski, S., and Kähler, C., "Investigation of a Generic Space Launcher Wake in Sub-, Trans- and Supersonic Conditions," Sonderforschungsbereich/Transregio 40 (SFBTR40)–Annual Report, 2016.

[25] van Oudheusden, B. W., "PIV-Based Pressure Measurement," *Measurement Science and Technology*, Vol. 24, 2013, Paper 032001. doi:10.1088/0957-0233/24/3/032001

[26] van Gent, P. L., van Oudheusden, B. W., and Schrijer, F. F. J., "Determination of Mean Pressure from PIV in Compressible Flows Using the Reynolds-Averaging Approach," *Experiments in Fluids*, Vol. 59, March 2018, Paper 41. doi:10.1007/s00348-018-2487-2

[27] Schrijer, F. F. J., Sciacchitano, A., and Scarano, F., "Spatio-Temporal and Modal Analysis of Unsteady Fluctuations in a High-Subsonic Base Flow," *Physics of Fluids*, Vol. 26, No. 8, 2014, Paper 086101. doi:10.1063/1.4891257

[28] Meliga, P., and Reijasse, P., "Unsteady Transonic Flow Behind an Axisymmetric Afterbody Equipped with Two Boosters," *25th AIAA Applied Aerodynamics Conference*, AIAA Paper 2007-4564, 2007. doi:10.2514/6.2007-4564

[29] Stephan, S., and Radespiel, R., "Propulsive Jet Simulation with Air and Helium in Launcher Wake Flows," *CEAS Space Journal*, Vol. 9, No. 2, 2017, pp. 195–209. doi:10.1007/s12567-016-0142-4

[30] Schreyer, A.-M., Stephan, S., and Radespiel, R., "Characterization of the Supersonic Wake of a Generic Space Launcher," *CEAS Space Journal*, Vol. 9, No. 1, 2017, pp. 97–110. doi:10.1007/s12567-016-0134-4

[31] Hirschel, E., "Vehicle Design and Critical Issues; FESTIP Technology Development Work in Aerothermodynamics for Reusable Launch Vehicles," *ESA/ESTEC FESTIP Workshop*, Noordwijk, The Netherlands, 1996.

[32] Bannink, W., Houtman, E., and Bakker, P., "Base Flow/Underexpanded Exhaust Plume Interaction in a Supersonic External Flow," *8th AIAA International Space Planes and Hypersonic Systems and Technologies Conference*, AIAA Paper 1998-1598, 1998. doi:10.2514/6.1998-1598

[33] Bakker, P., Bannink, W., Servel, P., and Reijasse, P., "CFD Validation for Base Flows With and Without Plume Interaction," *40th AIAA Aerospace Sciences Meeting and Exhibit*, AIAA Paper 2002-0438, 2002. doi:10.2514/6.2002-438

[34] van Oudheusden, B. W., and Scarano, F., "PIV Investigation of Supersonic Base-Flow–Plume Interaction," *Topics in Applied Physics*, Vol. 112, Springer, Berlin, 2008, pp. 465–474. doi:10.1007/978-3-540-73528-1_25

[35] Stephan, S., Wu, J., and Radespiel, R., "Propulsive Jet Influence on Generic Launcher Base Flow," *CEAS Space Journal*, Vol. 7, No. 4, 2015, pp. 453–473. doi:10.1007/s12567-015-0098-9

[36] Papamoschou, D., and Roshko, A., "The Compressible Turbulent Shear Layer: An Experimental Study," *Journal of Fluid Mechanics*, Vol. 197, Dec. 1988, pp. 453–477. doi:10.1017/S0022112088003325

[37] Smits, A. J., and Dussauge, J.-P., *Turbulent Shear Layers in Supersonic Flow*, Springer, New York, 2006. doi:10.1007/b137383

[38] Musial, N. T., and Ward, J. J., "Base Flow Characteristics for Several Four-Clustered Rocket Configurations at Mach Numbers from 2.0 to 3.5," NASA TR TN-D-1093, 1961.

[39] Peters, W., "An Evaluation of Jet Simulation Parameters for Nozzle Afterbody Testing at Transonic Mach Numbers," ARO, Inc., Arnold Air Force Station, Final Rept. TN, 1976.

[40] Peters, W. L., "Jet Simulation Techniques: Simulation of Temperature Effects by Altering Gas Composition," ARO, Inc., Arnold Air Force Station, Final Rept. TN, 1977.

[41] Zapryagaev, V., Lokotko, A., Nikiforov, S., Pavlov, A., Tchernyshev, A., Bannink, W., Ottens, H., and Muylaert, J., "Experimental Investigation of Base Pressure with Hot Supersonic Jet for External Supersonic Flow," *Fourth Symposium on Aerothermodynamics for Space Vehicles: Co-sponsored by European Space Agency*, edited by R. A. Harris, European Space Agency, Capua, Italy, 2002, p. 579.

[42] Stephan, S., Radespiel, R., and Müller-Eigner, R., "Jet Simulation Facility Using the Ludwieg Tube Principle," *5th European Conference for Aeronautics and Space Sciences (EUCASS)*, Munich, Germany, July 2013.

[43] Saile, D., Kirchheck, D., Ali, G., and Banuti, D., "Design of a Hot Plume Interaction Facility at DLR Cologne," *Proceedings of the 8th European Symposium on Aerothermodynamics for Space Vehicles*, ESA, March 2015.

[44] Blinde, P., Gentile, V., van Oudheusden, B., and Schrijer, F., "Determination of Instantaneous Pressure Fields in a Low-Speed Axisymmetric Base Flow Based on Time-Resolved Tomographic PIV," *NIOPLEX International Workshop on Non-Intrusive Optical Flow Diagnostics Intrusive Measurements for Unsteady Flows and Aerodynamics*, Prime Institute, Poitiers, France, Oct. 2015.

[45] Schrijer, F. F. J., Scarano, F., and van Oudheusden, B. W., "Application of PIV in a Mach 7 Double-Ramp Flow," *Experiments in Fluids*, Vol. 41, No. 2, 2006, pp. 353–363. doi:10.1007/s00348-006-0140-y

[46] Ragni, D., Schrijer, F., van Oudheusden, B. W., and Scarano, F., "Particle Tracer Response Across Shocks Measured by PIV," *Experiments in Fluids*, Vol. 50, No. 1, 2011, pp. 53–64. doi:10.1007/s00348-010-0892-2

[47] Westerweel, J., and Scarano, F., "Universal Outlier Detection for PIV Data," *Experiments in Fluids*, Vol. 39, No. 6, 2005, pp. 1096–1100. doi:10.1007/s00348-005-0016-6

[48] Gurka, R., Liberzon, A., Rubinstein, D., and Shavit, U., "Computation of Pressure Distribution Using PIV Velocity Data," *3rd International Workshop on Particle Image Velocimetry*, edited by R. Adrian, Y. Hassan, and C. Meinhart, Santa Barbara, CA, Sept. 1999.

[49] van Oudheusden, B. W., Scarano, F., Roosenboom, E. W. M., Casimiri, E. W. F., and Souverein, L. J., "Evaluation of Integral Forces and Pressure Fields from Planar Velocimetry Data for Incompressible and Compressible Flows," *Experiments in Fluids*, Vol. 43, Nos. 2–3, 2007, pp. 153–162. doi:10.1007/s00348-007-0261-y

[50] van Oudheusden, B. W., "Principles and Application of Velocimetry-Based Planar Pressure Imaging in Compressible Flows with Shocks," *Experiments in Fluids*, Vol. 45, No. 4, 2008, pp. 657–674. doi:10.1007/s00348-008-0546-9

[51] Jeon, Y. J., Chatellier, L., Beaudoin, A., and David, L., "Least-Square Reconstruction of Instantaneous Pressure Field Around a Body Based on a Directly Acquired Material Acceleration in Time-Resolved PIV," *11th International Symposium on Particle Image Velocimetry-PIV15*, Santa Barbara, CA, Sept. 2015.

[52] van Gent, P. L., Michaelis, D., van Oudheusden, B. W., Weiss, P. É., de Kat, R., Laskari, A., Jeon, Y. J., David, L., Schanz, D., Huhn, F., et al., "Comparative Assessment of Pressure Field Reconstructions from Particle Image Velocimetry Measurements and Lagrangian Particle Tracking," *Experiments in Fluids*, Vol. 58, April 2017, Paper 33. doi:10.1007/s00348-017-2324-z

[53] Adrian, R., and Westerweel, J., *Particle Image Velocimetry*, Cambridge Univ. Press, New York, 2011. doi:10.1017/S0001924000006734

[54] Raffel, M., Willert, C. E., Wereley, S. T., and Kompenhans, J., *Particle Image Velocimetry*, 2nd ed., Experimental Fluid Mechanics, Springer, Berlin, 2007. doi:10.1007/978-3-540-72308-0

[55] Sciacchitano, A., Neal, D. R., Smith, B. L., Warner, S. O., Vlachos, P. P., Wieneke, B., and Scarano, F., "Collaborative Framework for PIV Uncertainty Quantification: Comparative Assessment of Methods," *Measurement Science and Technology*, Vol. 26, 2015, Paper 074004. doi:10.1088/0957-0233/26/7/074004

[56] Samimy, M., and Lele, S. K., "Motion of Particles with Inertia in a Compressible Free Shear Layer," *Physics of Fluids A*, Vol. 3, No. 8, 1991, pp. 1915–1923. doi:10.1063/1.857921

[57] Wilson, B. M., and Smith, B. L., "Uncertainty on PIV Mean and Fluctuating Velocity due to Bias and Random Errors," *Measurement Science and Technology*, Vol. 24, 2013, Paper 035302. doi:10.1088/0957-0233/24/3/035302

[58] Sciacchitano, A., and Wieneke, B., "PIV Uncertainty Propagation," *Measurement Science and Technology*, Vol. 27, No. 8, 2016, Paper 084006. doi:10.1088/0957-0233/27/8/084006

[59] Simon, F., Deck, S., Guillen, P., Sagaut, P., and Merlen, A., "Numerical Simulation of the Compressible Mixing Layer Past an Axisymmetric Trailing Edge," *Journal of Fluid Mechanics*, Vol. 591, 2007, pp. 215–253. doi:10.1017/S0022112007008129

[60] Eaton, J. K., and Johnston, J. P., "Low Frequency Unsteadyness of a Reattaching Turbulent Shear Layer," *Turbulent Shear Flows 3*, edited by L. J. S. Bradbury, F. Durst, B. E. Launder, F. W. Schmidt, and J. H. Whitelaw, Springer, Berlin, 1982, pp. 162–170.

[61] Giepman, R. H. M., Schrijer, F. F. J., and van Oudheusden, B. W., "High-Resolution PIV Measurements of a Transitional Shock Wave–Boundary Layer Interaction," *Experiments in Fluids*, Vol. 56, June 2015, Paper 113.
doi:10.1007/s00348-015-1977-8

[62] Statnikov, V., Glatzer, C., Meiß, J.-H., Meinke, M., and Schröder, W., "Numerical Investigation of the Near Wake of Generic Space Launcher Systems at Transonic and Supersonic Flows," *Progress in Flight Physics*, Vol. 5, edited by P. Reijasse, D. Knight, M. Ivanov, and I. Lipatov, EDP Sciences, Les Ulis, France, 2013, pp. 191–208.
doi:10.1051/eucass/201305191

[63] Stephan, S., Wu, J., and Radespiel, R., "Propulsive Jet Influence on Generic Launcher Base Flow," *CEAS Space Journal*, Vol. 7, No. 4, 2015, pp. 453–473.
doi:10.1007/s12567-015-0098-9

[64] Herrin, J. L., and Dutton, J. C., "Supersonic Base Flow Experiments in the Near Wake of a Cylindrical Afterbody," *AIAA Journal*, Vol. 32, No. 1, 1994, pp. 77–83.
doi:10.2514/3.11953

D. Papamoschou
Associate Editor